

# Supplementary Information

## Wirtinger Holography for Near-eye Displays

PRANEETH CHAKRAVARTHULA, University of North Carolina at Chapel Hill

YIFAN PENG, Stanford University

JOEL KOLLIN, Microsoft Research

HENRY FUCHS, University of North Carolina at Chapel Hill

FELIX HEIDE, Princeton University

CCS Concepts: • **Hardware** → **Emerging optical and photonic technologies**; • **Applied computing** → **Physics**; • **Human-centered computing** → **Displays and imagers**; • **Computing methodologies** → **Computer graphics**.

Additional Key Words and Phrases: computer generated holography, near-eye display, augmented reality, virtual reality, vergence-accommodation conflict, computational displays

### ACM Reference Format:

Praneeth Chakravarthula, Yifan Peng, Joel Kollin, Henry Fuchs, and Felix Heide. 2019. Supplementary Information Wirtinger Holography for Near-eye Displays. *ACM Trans. Graph.* 38, 6, Article 213 (November 2019), 15 pages. <https://doi.org/10.1145/3355089.3356539>

In this document we provide additional derivations and results in support of the main manuscript.

### 1 INTRODUCTION TO WIRTINGER CALCULUS

In this section, we provide a quick introduction to Wirtinger calculus and Wirtinger derivatives in the context of optimization problems which involve derivatives of a complex variable. However, we refer interested readers to [Remmert 2012] for a detailed discussion on complex functions and analysis.

Consider a real-valued function of a real variable, for instance:

$$f : \mathbb{R} \ni x \mapsto y = f(x) \in \mathbb{R}, \quad (1)$$

the point  $x_{opt}$ , where  $f(x)$  is maximum (or minimum) is obtained by taking the derivative of  $f$  concerning  $x$  and setting it zero. In other words, for  $x_{opt}$ , the following equation has to be valid

$$\left. \frac{df}{dx} \right|_{x_{opt}} = 0. \quad (2)$$

---

Authors' addresses: Praneeth Chakravarthula, cpk@cs.unc.edu, University of North Carolina at Chapel Hill, Chapel Hill, NC; Yifan Peng, evanpeng@stanford.edu, Stanford University, Stanford, CA; Joel Kollin, jkollin@microsoft.com, Microsoft Research, Redmond, WA; Henry Fuchs, fuchs@cs.unc.edu, University of North Carolina at Chapel Hill, Chapel Hill, NC; Felix Heide, fheide@cs.princeton.edu, Princeton University, Princeton, NJ.

---

Permission to make digital or hard copies of all or part of this work for personal or classroom use is granted without fee provided that copies are not made or distributed for profit or commercial advantage and that copies bear this notice and the full citation on the first page. Copyrights for components of this work owned by others than the author(s) must be honored. Abstracting with credit is permitted. To copy otherwise, or republish, to post on servers or to redistribute to lists, requires prior specific permission and/or a fee. Request permissions from [permissions@acm.org](mailto:permissions@acm.org).

© 2019 Copyright held by the owner/author(s). Publication rights licensed to ACM.

0730-0301/2019/11-ART213 \$15.00

<https://doi.org/10.1145/3355089.3356539>

Note that here we assume  $f(x)$  to be continuous in some domain  $\mathbb{D}$ , and the derivative to exist. However, whether the obtained solution gives a maximum or minimum value needs to be checked using additional conditions or higher-order derivatives.

We can define the derivative for a complex function of a complex variable, for instance

$$f : \mathbb{C} \ni z \mapsto w = f(z) \in \mathbb{C}, \quad (3)$$

as follows

$$f'(z_0) = \left. \frac{df}{dz} \right|_{z_0} = \lim_{z \rightarrow z_0} \frac{f(z) - f(z_0)}{z - z_0}. \quad (4)$$

If  $f'(z)$  exists in the domain  $\mathbb{D} \subset \mathbb{R}$ , the function  $f(z)$  is called an *analytic* or a *holomorphic* function in  $\mathbb{R}$ .

Now, a given complex function can be decomposed into two real functions, each depending on two real variables, say  $x$  and  $y$ , which are the real and imaginary parts of the complex variable  $z$ . Mathematically, this can be represented as

$$f(z) = f(x + jy) \equiv u(x, y) + jv(x, y); z = x + jy \quad (5)$$

It can be shown that for the above function  $f(z)$  to be holomorphic, the corresponding component functions  $u(x, y)$  and  $v(x, y)$  need to satisfy the Cauchy-Riemann conditions [Remmert 2012]

$$\frac{\partial u(x, y)}{\partial x} = \frac{\partial v(x, y)}{\partial y} \quad (6)$$

$$\frac{\partial v(x, y)}{\partial x} = -\frac{\partial u(x, y)}{\partial y} \quad (7)$$

If the above conditions are valid, then the complex derivative of a holomorphic function  $f(z)$  can be expressed by the partial derivatives of the component real functions  $u(x, y)$  and  $v(x, y)$  as

$$\frac{df(z)}{dz} = \frac{\partial u(x, y)}{\partial x} + j \frac{\partial v(x, y)}{\partial x} \quad (8)$$

### 1.1 Real functions of complex variables

As mentioned in the main manuscript, it can be seen from Equation 8 that if the function  $f(z)$  is a real valued function, then the component function  $v(x, y)$  which forms the imaginary part of  $f(z)$  is zero, i.e.  $v(x, y) = 0$ . Following Cauchy-Riemann conditions as described in Equation 6, we see that

$$\frac{\partial u(x, y)}{\partial x} = \frac{\partial v(x, y)}{\partial y} = 0 \quad (9)$$

Thus,  $u(x, y)$  is always a constant, and so is the function  $f(z)$ , and the derivative of such a function is always zero. In other words, a real function of complex variable is not holomorphic unless it is a real constant.

To work around this, instead of treating  $f(z)$  as a real function of a complex variable, we regard  $f(z) = u(x, y)$  as a function of two real variables. In the context of solving an optimization problem, it can be treated as a multidimensional real function. Therefore, to find the optimum value of  $f(z)$ , we want to find the optimum of  $u(x, y)$ , which requires

$$\frac{\partial u(x, y)}{\partial x} = 0 \quad \text{and} \quad \frac{\partial u(x, y)}{\partial y} = 0 \quad (10)$$

Note that  $v(x, y) = 0$  since the function is real valued.

Both of the above real-valued equations for the optimal components  $x_{opt}$  and  $y_{opt}$  can be linearly combined into a more compact one complex-valued representation as follows

$$\alpha_1 \frac{\partial u(x, y)}{\partial x} + j \alpha_2 \frac{\partial u(x, y)}{\partial y} = 0 + j0 = 0 \quad (11)$$

where  $\alpha_1$  and  $\alpha_2$  are arbitrary real valued non-zero constants. Note that the above representation is valid since the real and imaginary parts are orthogonal, and the linear combination is only intended to devise a compact representation.

Let us now define a differential operator writing the real and imaginary parts of  $z = x + jy$  as the tuple  $(x, y)$

$$\frac{\partial}{\partial z} = \alpha_1 \frac{\partial}{\partial x} + j \cdot \alpha_2 \frac{\partial}{\partial y}. \quad (12)$$

Note that the operator defined in Equation 12 can also be applied to complex functions, because real cost functions can often be decomposed into complex components, for example  $f(z) = |z|^2 = z \cdot \bar{z} = f_1(z)f_2(z)$ , where  $f_1(z), f_2(z) \in \mathbb{C}$ . Also, observe that  $\bar{z} = x - jy$  is the complex conjugate of  $z = x + jy$ .

The choice of values  $\alpha_1 = \frac{1}{2}$  and  $\alpha_2 = -\frac{1}{2}$  meets the requirements for defining the complex derivatives, and it was first introduced by *Wilhelm Wirtinger*. Wirtinger derivatives of a (complex) function  $f(z)$  of a complex variable  $z = x + jy$  are defined as the following linear partial differential operators of the first order

$$\frac{\partial f}{\partial z} = \frac{1}{2} \cdot \left( \frac{\partial f}{\partial x} - j \cdot \frac{\partial f}{\partial y} \right) \quad (13)$$

and

$$\frac{\partial f}{\partial \bar{z}} = \frac{1}{2} \cdot \left( \frac{\partial f}{\partial x} + j \cdot \frac{\partial f}{\partial y} \right) \quad (14)$$

For functions of many variables,  $f : \mathbb{C}^n \ni z = [z_1, z_2, \dots, z_n]^T \mapsto w = f(z) \in \mathbb{R}$ , all  $n$  partial derivatives with respect to the complex variables  $z_1, \dots, z_n$  need to be calculated. In other words, the derivatives need to be calculated and combined into a vector again, and this *gradient* of the function can be defined as follows

$$\frac{\partial f}{\partial z} = \begin{bmatrix} \frac{\partial f}{\partial z_1} \\ \frac{\partial f}{\partial z_2} \\ \vdots \\ \frac{\partial f}{\partial z_n} \end{bmatrix} \quad \text{and} \quad \frac{\partial f}{\partial \bar{z}} = \begin{bmatrix} \frac{\partial f}{\partial \bar{z}_1} \\ \frac{\partial f}{\partial \bar{z}_2} \\ \vdots \\ \frac{\partial f}{\partial \bar{z}_n} \end{bmatrix} \quad (15)$$

Of course, the Wirtinger gradients defined in Equation 15 has to be equal to the zero vector  $\mathbf{0} = [0, 0, \dots, 0]^T$ . Note that for such multidimensional functions, one can separate and inspect individually the real and imaginary parts. But using the above definition, we can use simple arithmetic rules that can be expressed using vectors and matrices. This flexibility allows us to use formal optimization methods easily.

## 2 ADDITIONAL DISCUSSION ON IMAGE FORMATION MODELS

In this section, we describe additional propagation models which can be incorporated by the proposed method.

### 2.1 Fourier transform-based propagation

A further simplification, in addition to the convolutional approximation from the main manuscript, is a parabolic approximation that can be made to remove the square root operation in the Euclidean distance term in Equation 2 in the main manuscript to obtain a more convenient Fresnel scalar diffraction model. However, this propagation constrains the sampling on the image plane, which is determined by the wavelength and propagation distance from the hologram. Also, the sampling pattern on the image plane is restricted by the sampling pattern on the hologram plane, and vice-versa. This constrained sampling is an issue when the hologram and image planes are of different sizes, especially for near-eye displays which may use spherical wave illumination for supporting wide field-of-view [Maimone et al. 2017; Shi et al. 2017].

One can overcome the sampling limitation by employing a two-step Fresnel propagation using an intermediate observation plane to effectively decouple the sampling on both hologram and image planes [Okada et al. 2013]. For a sufficiently large distance of the intermediate plane from the hologram plane, we can further simplify the computation by employing Fraunhofer diffraction. The Fraunhofer-Fresnel two-step propagation results in optical wave field on the image plane as obtained by:

$$\begin{aligned}
 U_I(x, y) = & \underbrace{\frac{1}{\lambda^2 D(L+D)} \mathbf{exp} \left\{ \frac{jk}{2(L+D)} [x^2 + y^2] \right\}}_{E_3} \\
 & \mathcal{F} \left\{ \underbrace{\mathbf{exp} \left\{ \frac{jk}{-2D} [\zeta^2 + \eta^2] \right\}}_{E_2} \right. \\
 & \left. \mathcal{F}^{-1} \left\{ U_H(\zeta, \eta) \right\} \underbrace{\mathbf{exp} \left\{ \frac{jk}{2(L+D)} [\zeta^2 + \eta^2] \right\}}_{E_1} \right\}, \tag{16}
 \end{aligned}$$

where  $L$  and  $D$  are distances to the image plane and intermediate plane from the hologram plane respectively,  $k$  is the wave number,  $U_H(\zeta, \eta)$  and  $U_I(x, y)$  are the optical wave fields on the hologram and image plane respectively. For brevity, the above equation can be expressed as:

$$U_I(x, y) = E_3 \circ \mathcal{F}(E_2 \circ (\mathcal{F}^{-1}(U_H)) \circ E_1). \tag{17}$$

## 2.2 Gradient for Fourier-transform based propagation

We discussed in the previous paragraphs that the field in the destination plane can be obtained as  $z = E_3 \circ \mathcal{F}(E_2 \circ (\mathcal{F}^{-1}U_H) \circ E_1)$  for a Fraunhofer-Fresnel two-step propagation. Following steps as detailed in the main manuscript for the gradient of the convolutional model, the gradient of the loss function  $Err(\Phi)$  concerning  $\Phi$  can be computed as:

$$\nabla Err(\Phi) = Re(-je^{-j\phi} F E_1^* E_2^* F^\dagger E_3^* \nabla f). \tag{18}$$

## 2.3 Band-limited angular spectrum propagation

The diffractive field from the SLM, if Fourier-analyzed across any plane, can be identified as plane waves traveling in different directions away from the hologram plane. The field amplitude across any point can be calculated as the summation of contributions of these plane waves, taking into account the phase shifts undergone during the propagation [Goodman 2005]. This is called the *angular spectrum propagation* of the wave field. The angular spectrum method (ASM) is equivalent to the Rayleigh-Sommerfeld solution and yield identical predictions of the diffracted wave field [Shen and Wang 2006]. The ASM propagated field  $U_2(x, y; z)$  from a diffracting aperture with an input source field  $U_1(x, y; 0)$  can be computed as:

$$U_2(x, y; z) = \mathcal{F}^{-1} \left( \mathcal{F} U_1(x, y; 0) \circ H \right). \tag{19}$$

where  $H$  is the ASM transfer function given by:

$$H(f_x, f_y; z) = \begin{cases} \exp \left[ j2\pi \frac{z}{\lambda} \sqrt{1 - (\lambda f_x)^2 - (\lambda f_y)^2} \right] & , \quad \sqrt{f_x^2 + f_y^2} < \frac{1}{\lambda} \\ 0 & , \quad \text{otherwise} \end{cases} \tag{20}$$

Further, the angular spectrum transfer function can be band-limited to avoid numerical errors due to the sampling [Matsushima and Shimobaba 2009].

## 2.4 Gradient for ASM propagation

As discussed in previous paragraphs, the wave field at the destination plane can be obtained as  $z = \mathcal{F}^{-1}(\mathcal{F}U_1 \circ H)$ , and the image is computed as  $|z|^2$ . Computing Part 2 from the Part 1 gradient computed in Equation 9 in the main manuscript yields:

$$\begin{aligned} d(\text{Err}(H)) &= \text{Re}\langle \nabla f, dz \rangle \\ &= \text{Re}\langle \nabla f, d(F^\dagger(H)(FU_1)) \rangle \\ &= \text{Re}\langle \nabla f, F^\dagger H F dU_1 \rangle \\ &= \text{Re}\langle F^\dagger H^\dagger F \nabla f, dH \rangle \\ &= \text{Re}\langle F^\dagger H^* F \nabla f, dH \rangle \end{aligned} \quad (21)$$

Finally evaluating Part 3 with  $U_1 = \mathbf{exp}^{j\Phi}$ , we derive the definition of gradient of the loss function with respect to the phase  $\Phi$  as follows:

$$\begin{aligned} d(\text{Err}(\Phi)) &= \text{Re}\langle F^\dagger H^* F \nabla f, d(e^{j\phi}) \rangle \\ &= \text{Re}\langle -je^{-j\phi} F^\dagger H^* F \nabla f, d(\phi) \rangle \end{aligned} \quad (22)$$

Since the phase  $\Phi$  is real valued, the above inner-product definition can be read as:

$$d(\text{Err}(\Phi)) = \langle \text{Re}(-je^{-j\phi} F^\dagger H^* F \nabla f), d(\phi) \rangle, \nabla \text{Err}(\Phi) = \text{Re}(-je^{-j\phi} F^\dagger H^* F \nabla f). \quad (23)$$

## 2.5 Comparison with other gradient definitions

Note that the Wirtinger gradient definitions for various propagation models are coherent with the other definitions. For example, we consider the gradients derived by Fienup [Fienup 1993] for an  $\ell_2$  error metric. For the squared difference in intensities (squared magnitudes), the derivative with respect to a parameter  $p$  is defined as follows

$$\frac{\partial E}{\partial p} = 4\text{Re}\left(\sum_{x_1} \frac{\partial g(x_1)}{\partial p} \{P^\dagger[|G(u)|^2 |G^*(u) - |F(u)|^2 G^*(u)]\}^*\right), \quad (24)$$

where  $g(x)$  is the optical wavefront immediately after the input plane,  $G(u)$  is the wavefront at the detector plane,  $P$  is the propagation function and  $|F(u)|$  is the magnitude of the complex optical field at the detector. The above equation can be reformulated as

$$\frac{\partial E}{\partial p} = \text{Re}\left(\sum_{x_1} \frac{\partial g(x_1)}{\partial p} \{P^\dagger[2(|G(u)|^2 - |F(u)|^2) \cdot 2G^*(u)]\}^*\right). \quad (25)$$

It can be observed that the above formulation is consistent with the Wirtinger derivatives defined in the main manuscript, where  $[2(|G(u)|^2 - |F(u)|^2) \cdot 2G(u)]$  form Part 1 of Equation 9 defined in the main manuscript. Applying inverse propagation to the above equation and taking its conjugate becomes Part 2 of the chain rule, and finally multiplying with  $\frac{\partial g(x)}{\partial p}$  for any parameter  $p$ ; in our case phase  $\phi$ , where  $g(x) = \mathbf{exp}(j\phi)$ ; completes Part 3 of Equation 9.

## 3 OPTIMIZING FOR 3D HOLOGRAMS

The proposed Wirtinger holography framework can be extended to computing 3D holograms in a multi-layered or multi-focal approach. Given a 3D model or the scene data, one can voxelize and remap it into multiple depth planes. The hologram corresponding to each depth plane can be computed separately and all holograms can be later superposed to generate a complex hologram of the 3D scene. However, such an approach might not result in the optimal 2D phase pattern that generates the underlying 3D scene. Another approach is to jointly optimize for all depth planes to generate the corresponding optimal 2D hologram, which, however, is a challenging problem, as we will highlight next.

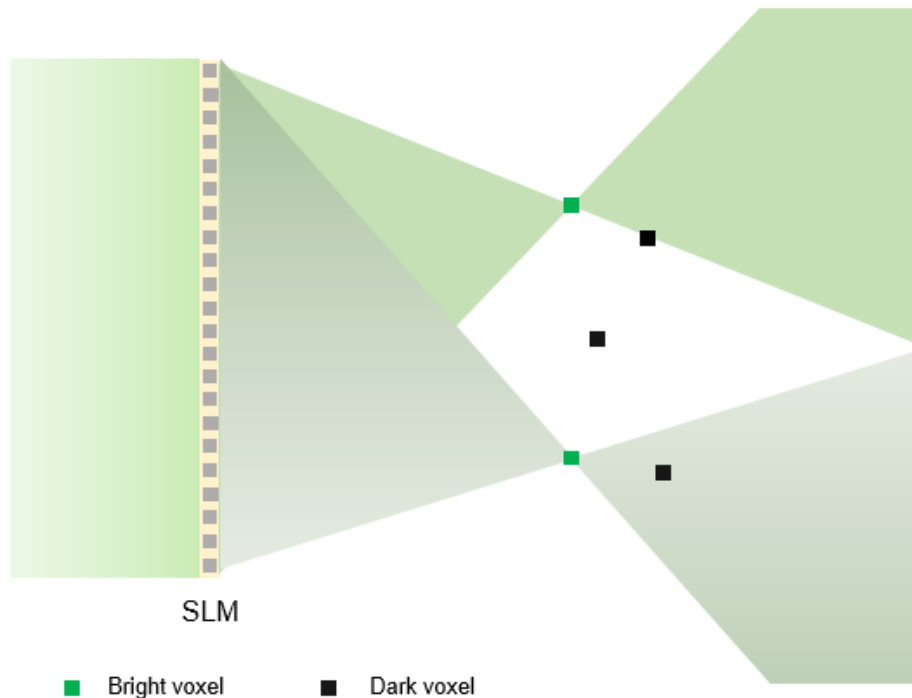


Fig. 1. Complications in computing a high quality 3D hologram. It is difficult to simultaneously create closely spaced bright and dark voxels in space with high fidelity. Creating a dark voxel immediately after a bright voxel, for any 3D hologram, requires rapid change in phase and is infeasible for a free space propagation.

As shown in Figure 1, let us suppose we have to create a few bright voxels and a few dark voxels in a 3D volume. When the SLM is illuminated by a collimated beam, the SLM pixels diffract light to focus at points in space to create the bright voxels. Observe that a dark voxel that escapes any of the diffracted light paths are not difficult to create. However, it is difficult or impossible to create a dark spot in space immediately after creating a focused bright spot. This requires the phase of light to change very rapidly in between the bright and dark voxels, which is physically infeasible for a free space propagation. Therefore, simultaneously creating a 3D volume with rapidly varying intensity is a difficult problem. However, one can generate good quality 3D holograms for relatively less complicated scenes, but most often, all 3D holograms suffer from noise and loss in contrast due to the above mentioned problem.

Computing high quality holograms by jointly optimizing for all depth planes using our Wirtinger holography framework also suffer the above mentioned problem, since if the depth planes are densely spaced, the optimizer forces light to change its phase rapidly while propagating, to simultaneously create closely spaced bright and dark voxels which are sometimes physically not feasible. Therefore the optimal phase hologram that is generated might contain noise which can degrade the image quality in comparison to 2D holograms. Although all 3D holographic rendering methods suffer from these problems, the holograms computed using full Fresnel diffraction integral without paraxial approximation and heuristic encoding schemes might produce fewer artifacts than

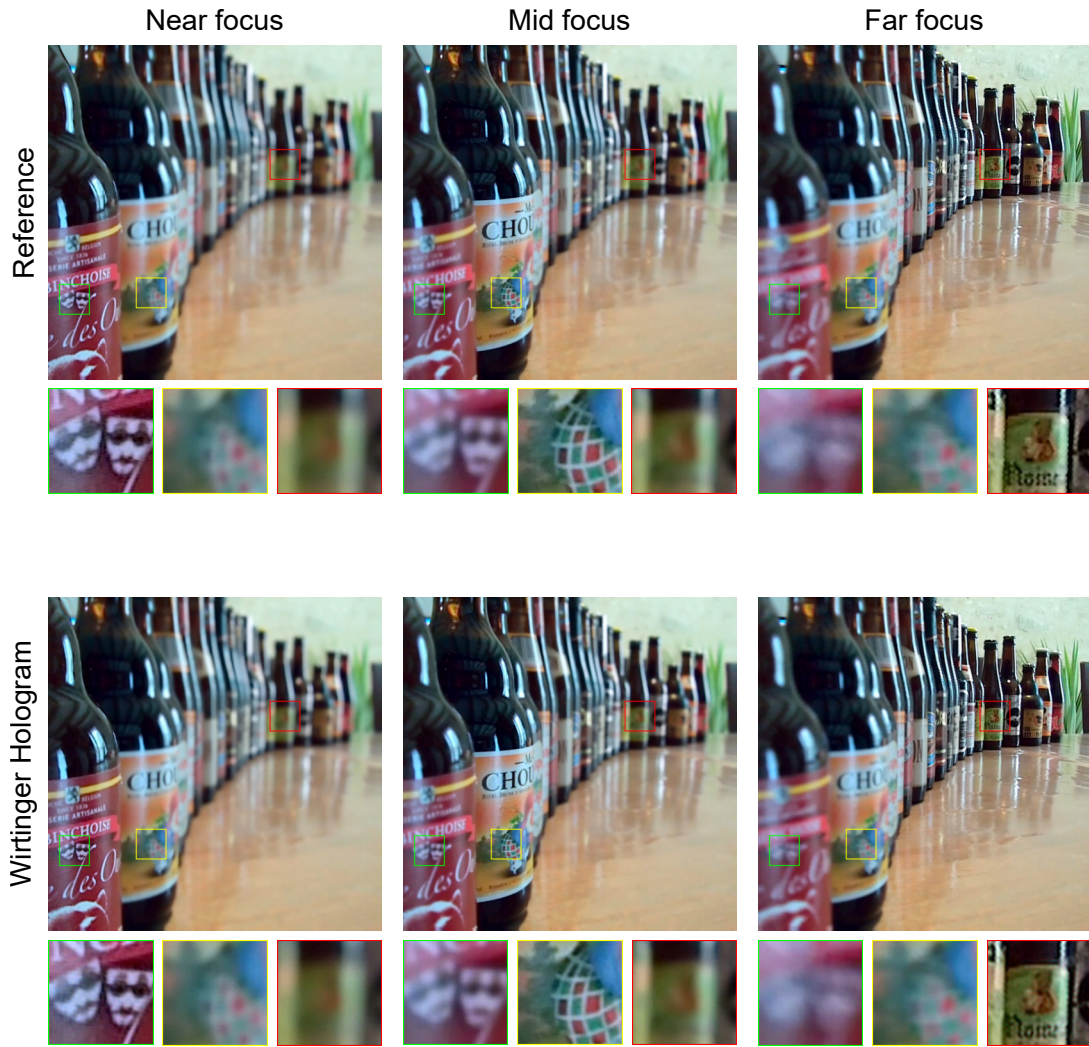


Fig. 2. Simulated holograms for a 3D scene generated using fast depth switching and dynamic global scene focus for an assumed eye tracked position. Observe that the depth of field effects are appropriately represented without compromising on the holographic image quality. The depth of the above scene is scaled to make the near distance at 200mm and far distance at 500mm. Image from the Lytro dataset.

optimizing for dense focal stack of 3D scene data. However, since the eye can only focus at one focal plane at a time, one can render holographic imagery at the eye accommodation plane by changing the scene focus globally. This needs to be accompanied by an eye tracker. Note, that although the depth detection capability progressively degrades with retinal eccentricity [Kim et al. 2017], object points which are closely spaced in the region where is eye is foveated suffer if not presented with an accurate depth of field blur [Maimone et al. 2017]. However, such regions can be addressed by providing the depth of field blur in the image space [Cholewiak et al. 2017]. Figure 2

shows simulated hologram results generated by our framework for a 3D scene by the method of dynamic global scene focus. Notice that the depth of field blur is appropriately represented without compromising on the image quality. Jointly optimizing for all depth planes to generate an artifact-free full 3D hologram remains an exciting direction for future work.

## 4 ADDITIONAL PROTOTYPE DETAILS

We built our bench-top prototype using cage system mounting. The optics are adjusted for an image plane distance of about 200 mm from the SLM. A Canon Rebel T6i DSLR camera is used to capture the holograms, without any camera lens present, but instead using a combination of two diffractive achromatic lenses as an eyepiece. Figure 3 shows the layout of our optical design.

We use red, green, and blue single-mode fiber lasers that are controlled by a Thorlabs LDC205C Laser Diode Controller, sequentially changing the three colors. The exposure of the imaging camera and the laser intensity are adjusted once based on the laser power. All capture settings are kept constant per experiments.

## 5 ADDITIONAL ANALYSIS OF IMPLEMENTATION

### 5.1 Initialization and Termination criteria

Here we discuss the initialization and termination criteria for the Wirtinger holography framework.

To solve Equation 8 of the main manuscript, we start the optimization process with an initial guess of the phase value  $\phi$ , which could either be a random phase or a carefully crafted phase. As mentioned in the main manuscript, carefully initializing the optimizer results in faster convergence compared to random (or shallow random) initialization. It can be easily understood from the main manuscript that the optimizer continuously searches for the optimal phase hologram for a given target intensity (image). However, one must note that there can be several phase holograms that can produce a given target intensity, making our objective function an extremely non-convex problem with several local minima. Therefore, initializing with a random phase distribution, intuitively, expands the search space for determining an optimal phase hologram. Owing to a larger domain of possible phase holograms, the particular choice of initial phase value may affect the convergence speed and numerical stability.

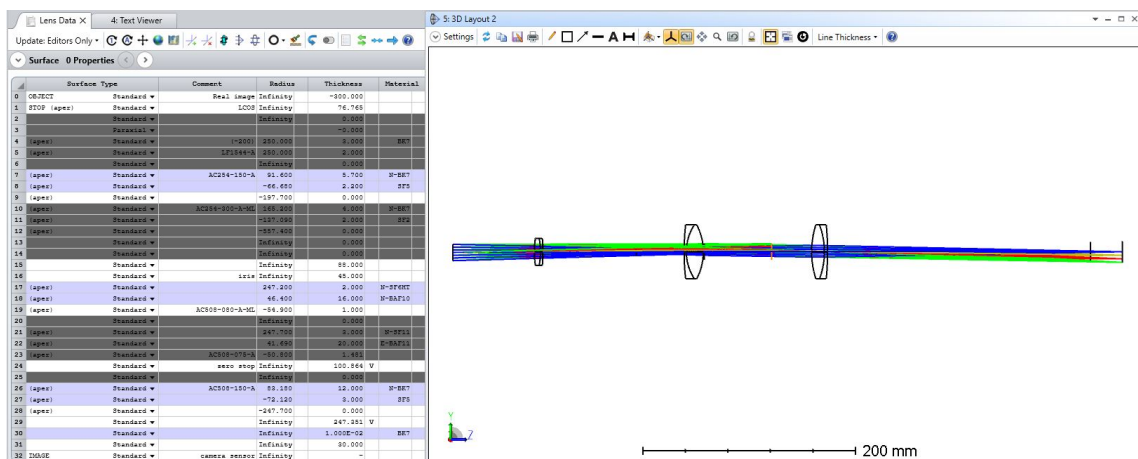


Fig. 3. An alternative optical design of the prototype near-eye display. Note that the laser source and its corresponding collimating optics are not shown here.

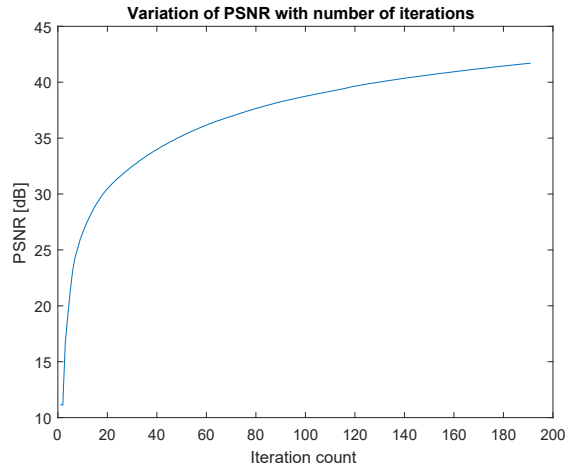


Fig. 4. PSNR values plotted against number of iterations for Wirtinger holography optimization for a randomly initialized phase.

Let us now consider one pixel on the hologram (SLM) plane. The complex amplitude of the hologram pixel constitutes a unit amplitude and a phase value lying in the range  $[0, 2\pi]$ . In other words, the complex amplitude of the hologram pixel can lie anywhere on a unit circle. Suppose if the phase is known to lie within a certain range  $[\alpha, \beta]$ , the correct complex number determining the complex amplitude of the hologram pixel must lie on an arc of the unit circle which is defined by the angles  $\alpha$  and  $\beta$ .

In our case, the possibility of the range of phase values for each hologram pixel remains unclear. However, given the knowledge of some initial phase value producing the target intensity pattern, it is reasonable to assume the optimal phase value might lie somewhere close to the initial phase value. Initializing the optimizer with a carefully crafted phase, for example, a few iterations of Gerchberg-Saxton algorithm or double-phase encoding, thus offers the promise of finding optimal phase faster. However, note that even with this additional information, the problem remains non-convex and cannot directly be efficiently solved. This can be reflected in the runtime values reported in the main manuscript, that careful initialization offers about 10 – 15s of speedup, but still takes a reasonable amount of time to achieve convergence. Figure 4 shows the PSNR values with iteration count for our framework for a randomly initialized phase, and it can be observed that the PSNR improves very quickly initially, and then slowly increases with an increasing number of iterations. For the results reported in the main manuscript, we terminate the optimizer once the PSNR values reach convergence.

## 5.2 Additional simulation results

As mentioned in the main manuscript, Wirtinger holography eliminates much of the ringing artifacts and generates high quality holographic reconstructions in comparison to the recently demonstrated modified GS and double phase encoding phase hologram generation algorithms. Figure 5 compares in simulation double phase encoding phase holograms and Wirtinger holograms, and present SSIM error maps as an indication of the probability of perceptually detecting ringing errors in the reconstructed image.

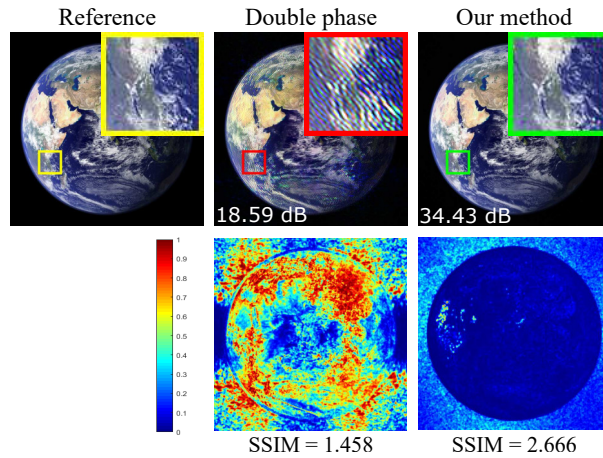


Fig. 5. Probability of detection of errors for the simulated image also shown in the main manuscript. Note that the Wirtinger holograms produce much less perceptual error as compared to that of double phase encoding method.

### 5.3 Cascaded holograms

In the main manuscript, we show that a cascaded SLM setup can generate superresolved holographic images. Figure 6 presents simulated images comparing holographic reconstructions of Wirtinger holograms obtained from a cascade of two low resolution  $960 \times 540$  phase-only SLMs, with the simulated holographic images of both double-phase and Wirtinger holograms obtained from a single high resolution  $1920 \times 1080$  phase-only SLM. Note that the holographic reconstruction obtained from a cascade of two low-resolution SLMs is superresolved in comparison to the holographic image obtained from a high-resolution double phase hologram. However, Wirtinger holograms from a single high-resolution SLM is better in quality compared to the holographic images from the cascaded low-resolution SLM.

### 5.4 Oversampled Phase Retrieval for Imaging

To further validate the flexibility of the proposed method, we also apply it to phase retrieval for imaging in Table 1. We adopt the  $4 \times$  oversampled phase retrieval problem setting discussed in [Metzler et al. 2018] without noise added in our case. We compare the baseline methods discussed in [Qian et al. 2017] and [Metzler et al. 2018] on a set of 10 standard images. Please see both references for additional details on the individual methods.

Table 1. Oversampled Phase Retrieval for Imaging. See text for details.

Method	PSNR [dB]
HIO	35.52
AltGD	35.85
TWF	35.33
MTWF	35.33
BSG	35.33
<b>This paper</b>	<b>36.34</b>

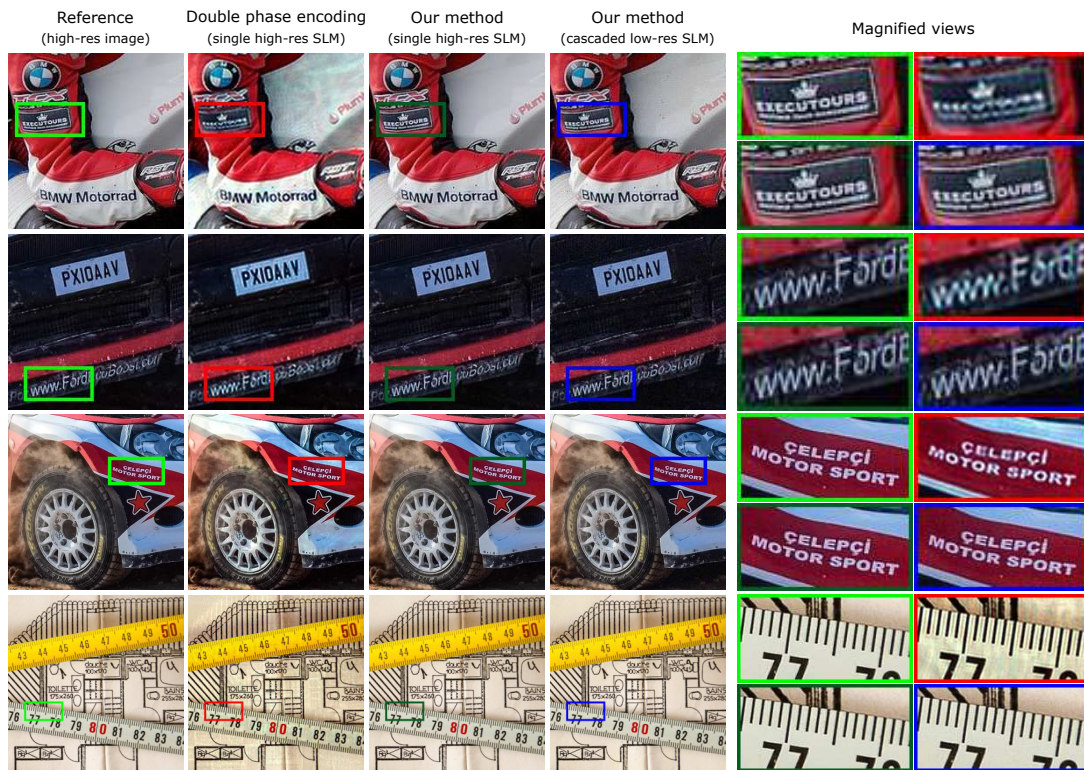


Fig. 6. Comparison of holographic images from a cascade of two low-resolution SLMs with hologram reconstructions of both double-phase and Wirtinger holograms from a high-resolution SLM. Note that the cascaded low resolution holograms are significantly better in quality compared to high resolution double phase holograms.

## 6 ADDITIONAL EXPERIMENTAL VALIDATION

### 6.1 Zero-order diffraction beam

We use Holoeye LETO-1 phase-only Spatial Light Modulator (SLM) with a  $6.4 \mu\text{m}$  pixel pitch and a 93% pixel fill factor. The fill factor describes the size of the non-functional dead area between two adjacent pixels of the SLM. The light that is incident on these dead areas is not modulated by the SLM and hence results in a zero-order diffraction beam (ZOD) on the optical axis. This ZOD introduces a high intensity illumination that distorts the desired light profile and undermines the hologram reconstruction quality.

A common solution to bypass the ZOD effects is to shift the illumination away from the optical axis, but this reduces the diffraction efficiency. To maintain high diffraction efficiency, we use an on-axis illumination in our hardware setup. Figure 7 presents images from our prototype display highlighting the zero-order diffracted light across all three color channels. Note that this zero-order pattern is a constant pattern across all the holographic images, causing deterioration in the image quality. As shown in Figure 8, if the ZOD is eliminated, the quality of Wirtinger holograms improve significantly

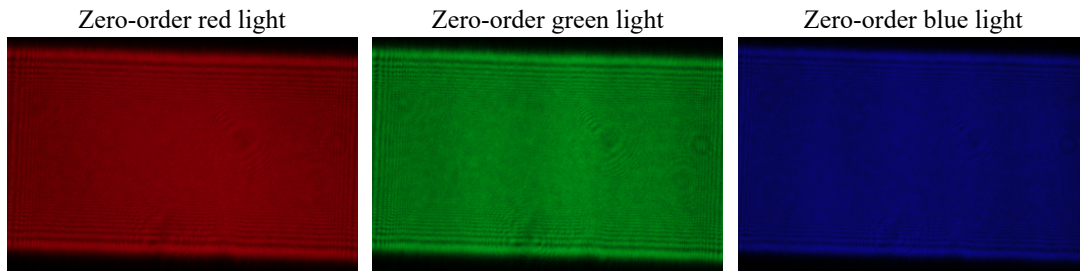


Fig. 7. Zero order diffracted light from the SLM for all three red, green and blue color lasers.



Fig. 8. Simulation of zero order filtering: Filtering the Zero order light improves the holographic image quality significantly.

## 6.2 SLM phase patterns

We show in Figure 9 the SLM phase patterns for the green laser of 517 nm used in our experimental setup for the phase-only hologram results presented in the main manuscript.

## 6.3 Hardware prototype results

We present several holographic images reconstructed on our prototype holographic display, other than the ones presented in the main manuscript, in Figure 10 and Figure 11. Wirtinger holograms feature more detail, higher resolution, and higher light efficiency.

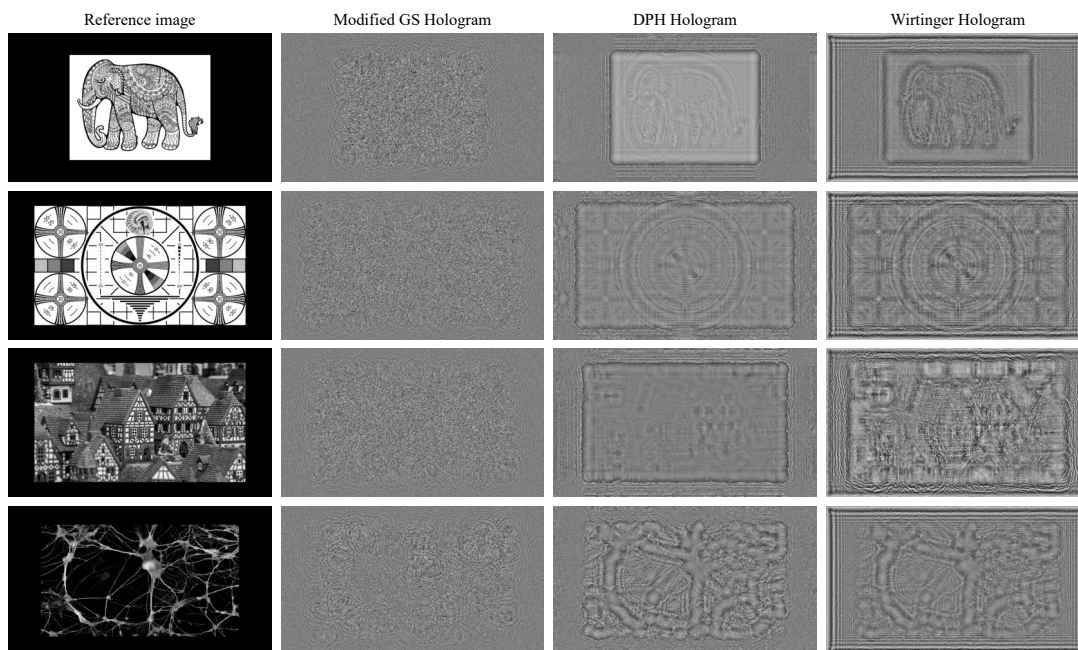


Fig. 9. Phase patterns of green channel for the images presented in the main manuscript.

## REFERENCES

- [n. d.]. On the formal theory of the functions of more complex ver author = Wirtinger, Wilhelm, journal = *Mathematical Annals*, volume = 97, number = 1, pages = 357-375, year = 1927, publisher = Springer. ([n. d.]).
- Steven A Cholewiak, Gordon D Love, Pratul P Srinivasan, Ren Ng, and Martin S Banks. 2017. ChromaBlur: Rendering chromatic eye aberration improves accommodation and realism. *ACM Transactions on Graphics (TOG)* 36, 6 (2017), 210.
- James R Fienup. 1993. Phase-retrieval algorithms for a complicated optical system. *Applied optics* 32, 10 (1993), 1737-1746.
- Joseph W Goodman. 2005. *Introduction to Fourier optics*. Roberts and Company Publishers.
- JooHwan Kim, Qi Sun, Fu-Chung Huang, Li-Yi Wei, David Luebke, and Arie Kaufman. 2017. Perceptual studies for foveated light field displays. *arXiv preprint arXiv:1708.06034* (2017).
- Andrew Maimone, Andreas Georgiou, and Joel S Kollin. 2017. Holographic near-eye displays for virtual and augmented reality. *ACM Transactions on Graphics (TOG)* 36, 4 (2017), 85.
- Kyoji Matsushima and Tomoyoshi Shimobaba. 2009. Band-limited angular spectrum method for numerical simulation of free-space propagation in far and near fields. *Optics express* 17, 22 (2009), 19662-19673.
- Christopher A Metzler, Philip Schniter, Ashok Veeraraghavan, and Richard G Baraniuk. 2018. prDeep: Robust Phase Retrieval with a Flexible Deep Network. In *International Conference on Machine Learning*. 3498-3507.
- Naohisa Okada, Tomoyoshi Shimobaba, Yasuyuki Ichihashi, Ryutaro Oi, Kenji Yamamoto, Minoru Oikawa, Takashi Kakue, Nobuyuki Masuda, and Tomoyoshi Ito. 2013. Band-limited double-step Fresnel diffraction and its application to computer-generated holograms. *Optics express* 21, 7 (2013), 9192-9197.
- Cheng Qian, Xiao Fu, Nicholas D Sidiropoulos, Lei Huang, and Junhao Xie. 2017. Inexact alternating optimization for phase retrieval in the presence of outliers. *IEEE Transactions on Signal Processing* 65, 22 (2017), 6069-6082.
- Reinhold Remmert. 2012. *Theory of complex functions*. Vol. 122. Springer Science & Business Media.
- Fabin Shen and Anbo Wang. 2006. Fast-Fourier-transform based numerical integration method for the Rayleigh-Sommerfeld diffraction formula. *Applied optics* 45, 6 (2006), 1102-1110.
- Liang Shi, Fu-Chung Huang, Ward Lopes, Wojciech Matusik, and David Luebke. 2017. Near-eye light field holographic rendering with spherical waves for wide field of view interactive 3d computer graphics. *ACM Transactions on Graphics (TOG)* 36, 6 (2017), 236.

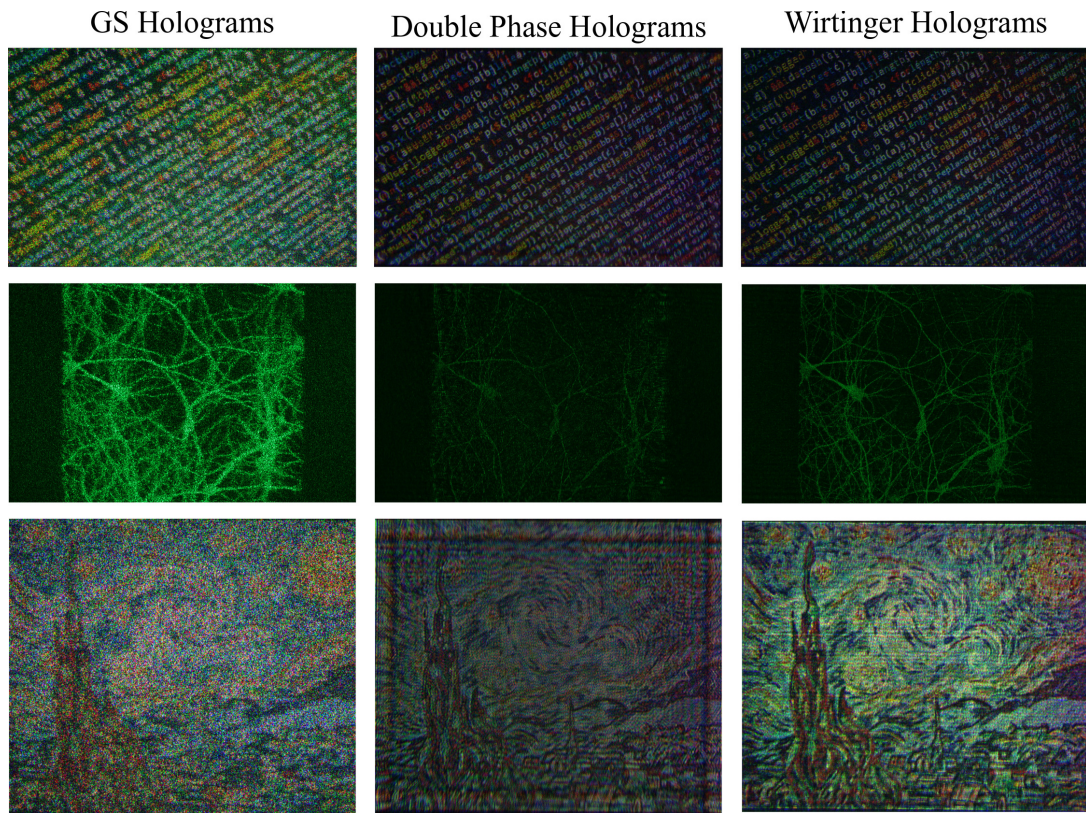


Fig. 10. Results reconstructed by modified GS holograms, Double phase encoding of Fresnel holograms, and Wirtinger Holograms. Neurons image by Karthik Krishnamurthy ©MBF Bioscience.

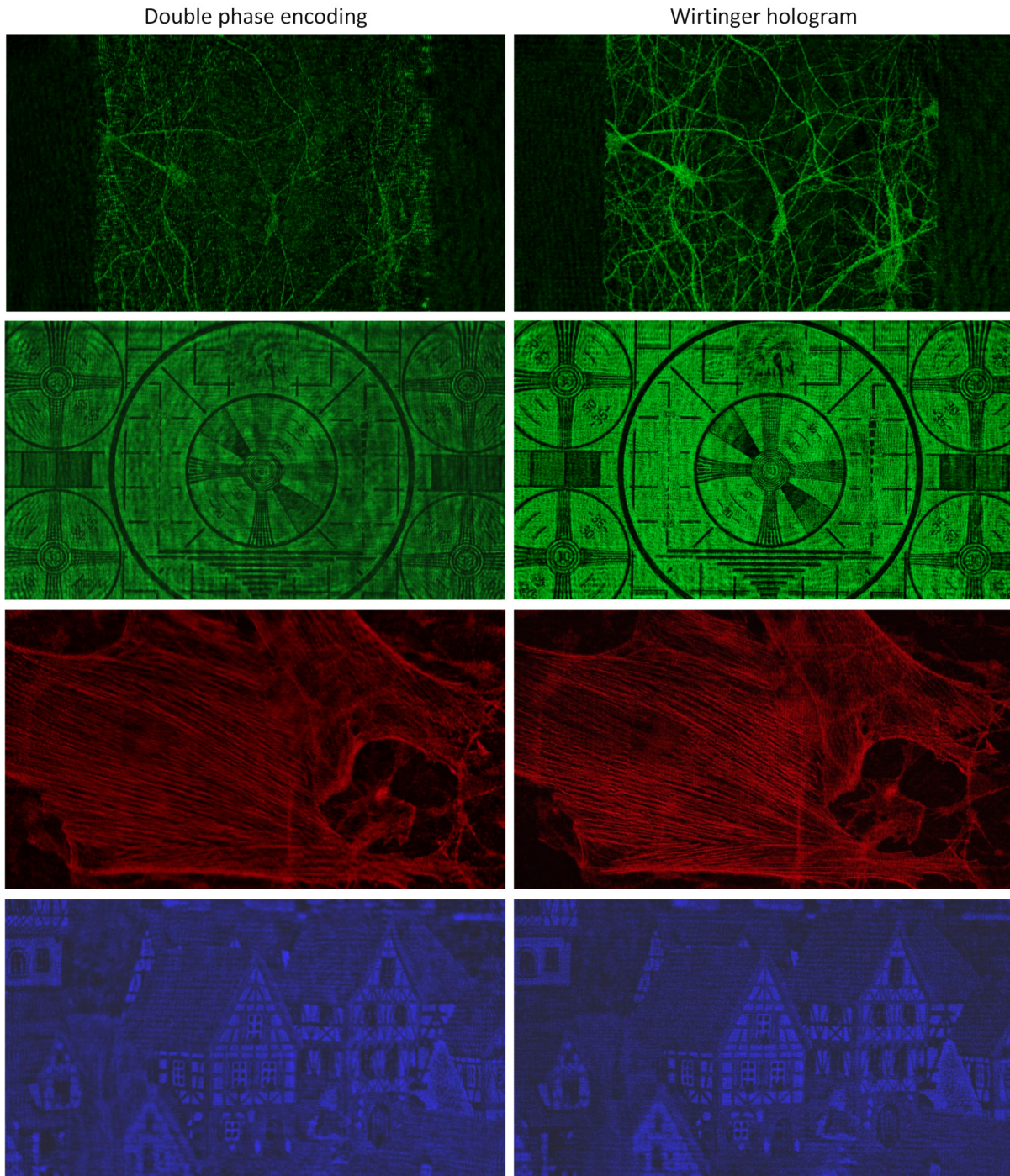


Fig. 11. Additional comparison of single color results generated by double phase encoding (left) and Wirtinger Holograms (right). We recommend the readers to zoom in for better viewing.